Chapter 5
High-Resolution PET/CT Development

Wai-Hoi Wong and Yuxuan Zhang

Abstract The main clinical application of positron emission tomography (PET) is in oncology, where it is used to diagnose malignant tumors, cancer staging, treatment response, follow-ups, and recurrence of diseases. The PET camera can detect therapeutic changes earlier than anatomical imaging modalities, because the structure being studied must significantly change in size and shape before it is detectable by the latter devices. Such important features of PET in oncology are, however, reduced by the image resolution and quality (noise) of clinical PET/CT systems, thereby limiting its effectiveness to diagnose lesions under a centimeter in size. Improving the PET image resolution and quality would enhance the oncologic efficacy of PET/CT by detecting smaller lesions with more accuracy of tracer uptake. It would also lead to earlier cancer detection, more accurate cancer staging, and more sensitive monitoring of treatment responses.

5.1 Introduction

The main clinical application of positron emission tomography (PET) is in oncology, where it is used to diagnose malignant tumors, cancer staging, treatment response, follow-ups, and recurrence of diseases. The PET camera can detect therapeutic changes earlier than anatomical imaging modalities, because the structure being studied must significantly change in size and shape before it is detectable by the latter devices. Such important features of PET in oncology are, however, reduced by the image resolution and quality (noise) of clinical PET/CT systems, thereby limiting its effectiveness to diagnose lesions under a centimeter in size. Improving the PET image resolution and quality would enhance the oncologic efficacy of PET/CT by detecting smaller lesions with more accuracy of tracer uptake. It would also lead to earlier cancer detection, more accurate cancer staging, and more sensitive monitoring of treatment responses.

W.-H. Wong (✉) • Y. Zhang
Department of Cancer Systems Imaging, The University of Texas MD, Anderson Cancer Center, 77030 Houston, TX, USA
e-mail: gwong@mdanderson.org

T. Inoue et al. (eds.), *Personalized Pathway-Activated Systems Imaging in Oncology*, DOI 10.1007/978-981-10-3349-0_5

The intrinsic spatial resolution of clinical PET or PET/CT systems has been limited to 4.5–6.5 mm in the last three decades. But recently, a 3 mm or better PET intrinsic spatial resolution has been achieved, with the advent of:

(a) L(Y)SO scintillation crystal that has higher light output and faster scintillation
(b) Small silicon photomultipliers (SiPM)
(c) Higher-resolution detector design, such as the PMT-quadrant-sharing (PQS) design
(d) Time-of-flight data acquisition and reconstruction
(e) Point-spread-function (PSF) iterative image reconstruction
(f) Larger axial field-of-view PET camera
(g) Localization of the depth of interaction of the gamma ray in the PET detectors

The new generation of clinical PET/CT incorporates some, but not all, of above advancements, which provides substantive PET/CT resolution to improve the application of PET for personalized oncology with more accurate tracer uptake quantification and diagnosis of smaller lesions. The ultimate incorporation of all the available advancements in future PET/CT systems can drive the molecular imaging capability of PET/CT to significantly higher levels for a better grasp and management of cancer. The technological tools to achieve higher levels of performance are discussed below.

5.2 Scintillation Crystals for High-Resolution PET/CT

The detector materials and how each material is used (detector design) fundamentally determine the intrinsic imaging resolution of PET. PET detectors require high effective atomic number (Z_{eff}) and high density (ρ) to effectively capture the energetic 511 KeV gamma rays for PET imaging. While the ability to stop the 511 KeV gamma rays in the detector is necessary for high-resolution PET imaging with narrow detector pixels, it is an insufficient condition should a gamma ray be absorbed in the detectors by multiple Compton scatterings. In such scenario, the energy signal would be distributed randomly over multiple neighboring crystals, thereby misreporting the first-entry location of the gamma ray. Thus for high-resolution PET imaging, the first detector interaction must have a high probability of photoelectric interactions (photofraction), which absorbs all the gamma energy at once. The photoelectric interaction probability is proportional to $(Z_{eff})^4$. The characteristics of some usable detector materials for the 511 KeV gamma detection [1–3] are listed in Table 5.1.

High Z_{eff} and photofraction (P) also provide high coincidence-detection sensitivity, as a function of P^2 because only photopeak events are accepted for the annihilation gamma rays to minimize the high scattered event noise in clinical PET images. Furthermore, high Z_{eff} and high stopping power materials have the lowest-resolution degradation caused by the uncertain depth of interaction (DOI), as thick detectors are needed to stop the 511 KeV gamma rays. From the above fundamental considerations

Table 5.1 Characteristics of PET detector materials for 511 KeV gamma rays

	BGO	L(Y)SO	NaI(Tl)	LaBr	CZT
Z_{eff}	75	66	51	50	50
Photofraction (P) of 1st interaction	43%	32%	19%	18%	18%
Light output (relative to NaI)	18	75	100	175	NA
Energy resolution	11%	12%	8%	3%	2%
Decay time (ns)	300	40	230	20	NA
Depth of Interaction blurring	Lowest	Moderate	High	High	High

of photofraction, sensitivity and DOI resolution degradation, for high resolution and high sensitivity, BGO is a good detector material, especially considering its low cost. Among the currently available detector materials, BGO can conceptually yield the highest resolution PET/CT if the scintillation light from each BGO pixel is detected by its own dedicated photosensor (1:1 coupling).

However, the current photosensor technology is limited to either the large size (18–50 mm) photomultiplier tubes (PMT) or the small (1–6 mm) but relatively costly silicon photomultipliers (SiPM). Notably, both hinder a 1:1 coupling between crystal pixels and photosensors. Coupling many crystals to a single photosensor would need the Anger positioning method for which the imaging resolution also depends on the light output of the scintillation crystal. The L(Y)SO crystal has four times the light output of the BGO and would provide higher spatial resolution when the Anger positioning is used for the detector design, despite its worse DOI blurring effect outside the field-of-view (FOV) center. In addition, the fast timing and high light output of LYSO can provide much more accurate timing of arrival for the gamma ray to 300–600 ps (Δx = 4.5–9 cm), which provides enough time-of-flight (TOF) information to improve the image signal-to-noise ratio by more than two times, especially for large patients. Hence, L(Y)SO is a good choice for high-resolution clinical PET/CT systems, despite its lower Z_{eff} and four times higher cost than BGO. However, for small FOV PET, such as brain, breast, and small-patient systems, where TOF is less beneficial and ultrahigh resolution and low cost are highly desirable, BGO crystals with 1:1 photosensor SiPM coupling would provide the highest-resolution imaging.

The fast scintillating LaBr crystal potentially has two times better TOF resolution than L(Y)SO and much better energy resolution for reducing scattered event noise [4, 5]. However, these two potential gains may not make up for its low coincidence photofraction-detection sensitivity that is 1/6 of BGO and 1/3 of that of L(Y)SO, for the same detector system geometry and axial FOV. CZT has the same coincidence photofraction-detection sensitivity disadvantage as LaBr and compounded by its poor timing that is inadequate to provide TOF information to enhance the image quality. Certainly, the LaBr and CZT system detection sensitivities can be increased by having a much larger axial FOV than BGO/LSO systems, but would increase the production cost. Both LaBr and CZT are expensive materials to grow, which limits the axial FOV of PET systems. The low 18% photofraction of the LaBr and CZT (low Z_{eff}) means that 82% of the gamma rays detected would be scattered

multiple times in the detectors, which would degrade the imaging resolution. In addition, the low stopping power also worsens the DOI image blurring effect. Hence, the LaBr and CZT are not ideal detector materials to make ultrahigh-resolution PET systems.

5.3 Solid-State Silicon Photomultiplier (SiPM) Photosensors

Traditionally, the scintillation light produced by the crystals is detected by photomultiplier tubes (PMT) and converted into electronic signals for the front-end electronics to process. The arrival of the silicon photomultipliers (SiPM) has provided a potentially exciting alternative to PMT in the design of high-resolution PET/CT systems because SiPM are small (1–3 mm square), thin, lightweight, resistant to high magnetic field, and much lower operating voltage. The disadvantages are higher noise, more temperature sensitive, and more costly to cover the same crystal footprint, at least for the time being. It needs 81–144 SiPM (3–4 mm in size) to replace a single 38-mm PMT. Due to lower gain and higher noise, each SiPM channel needs its own amplifier and supporting electronics. Replacing a PMT with a 100 SiPM increases the processing electronics by a 100-fold, which further increases the production cost and substantially increases the heat generation that requires much better cooling.

One advantage of SiPM is the small size that enables an ultrahigh-resolution PET system of 1–3 mm to be achieved without using analogy decoding schemes (Anger decoding) used by PMT systems. On the other hand, the best analog-decoding scheme using PMT can also achieve 1–3 mm resolution in animal and clinical systems [6, 7]. The second advantage of SiPM is its immunity to strong magnetic fields, thus making the PET/MR hybrid system a reality [8–10]. However, for PET/CT systems, PMT remains a viable low-cost choice while able to achieve very high resolution, approaching the fundamental PET resolution limit with the latest detector design presented in the next section.

5.4 The Fundamental PET Resolution Limits

Assuming the ideal detector system, the fundamental limit of PET image resolution is imposed by (a) the non-colinearity (0.5–0.54°) of the pair of 511 KeV gammas emitted, which is about 2 mm for the large clinical systems with 85 cm detector ring diameter and (b) the positron range of the tracer isotopes in water and the lung, as shown in Table 5.2 [11–12]. The non-colinearity effect originates from the Doppler effect of center-of-mass energy (E_c) of the short-lived positronium atom before the positron-electron annihilations; the FWHM of E_c is about 2.4 KeV [13]. The positron range is inversely proportional to the density of the surrounding tissues, which for the normal lung tissue is four times larger than soft tissues.

Table 5.2 Mean energy, maximum energy, and mean range of positron emitted

Isotopes	E_{mean} (KeV)	E_{max} (KeV)	R_{mean} (mm) water	R_{mean} (mm) lung
^{18}F	252	635	0.6	2.4
^{11}C	390	970	1.1	4.2
^{13}N	488	1190	1.5	5.8
^{15}O	730	1720	2.5	9.6
^{68}Ga	844	1899	2.9	11
^{62}Cu	1280	2926	6.1	23
^{82}Rb	1551	3378	5.9	23

Table 5.3 Fundamental resolution limits in water and lung for a whole-body PET

	^{18}F	^{11}C	^{13}N	^{15}O	^{68}Ga	^{62}Cu	^{82}Rb
PET resolution limit in water (mm)	2.1	2.3	2.5	3.2	3.5	6.4	6.2
PET resolution limit in lung (mm)	3.1	4.7	6.1	9.8	11.2	23.1	23.1

Table 5.4 Fundamental PET resolution limits of a dedicated brain PET (40-cm)

	^{18}F	^{11}C	^{13}N	^{15}O	^{68}Ga	^{62}Cu	^{82}Rb
PET resolution limit in water (mm)	1.1	1.4	1.8	2.7	3.0	6.2	6.0

The fundamental intrinsic PET resolution limits can be derived from Eq. 5.1. The fundamental resolution limit (FWHM) does not include the detector resolution:

$$\text{Fundamental resolution limit (FWHM)} = \left(R_{mean}{}^{2} + (0.0022 \text{ detector ring diameter})^{2}\right)^{\frac{1}{2}} \quad (5.1)$$

The fundamental intrinsic PET resolution limits in water-equivalent tissue and the lung is shown in Table 5.3 for different tracer isotopes.

For a large whole-body PET with F-18 tracers, such as FDG, FDOPA, F-Choline, FMISO, FLT, FAZA, and fluoride, the fundamental PET resolution is 2 mm in water-equivalent tissues and 3 mm in the lung. With the generator produced isotopes ^{68}Ga, ^{62}Cu, and ^{82}Rb, the fundamental PET resolution limits are in the range of 3.5–6 mm in water-equivalent tissues and 11–23 mm in the lung.

The fundamental PET resolution for a dedicated brain PET with a smaller 40-cm detection ring, assuming the ideal detector system, is shown in Table 5.4.

With F-18, the fundamental PET resolution is about 1 mm for a small dedicated brain PET system. With the generator produced Ga-68, the resolution limit is 3.0 mm. Hence, the small brain PET geometry can potentially improve PET resolution from 2 mm to 1 mm for F-18 tracers, but would not improve the resolution limit for the generator produced isotopes.

Current clinical PET/CT systems are whole-body systems with a detector ring diameter of 80–87 cm and use analog-decoding block detector designs. The typical image resolutions of these typical clinical PET systems are in the range of 4.5–6 mm, which is substantially worse than the fundamental PET resolution limits (2–3 mm), shown above for the cyclotron-generated isotopes, especially for the F-18 tracers.

Thus substantially higher-resolution PET imaging, with the resolution size reduced by two times or more, can be realized if (a) cost-effective higher-resolution PET detector designs are achievable and (b) the count collected is proportionally increased by 2^3 times or more. The increase in collected counts is necessary because, unlike CT, PET imaging is a count-deficient imaging modality with the image quality fundamentally determined by the statistical noise (photon statistical variations) in the signals obtained by the detector system. To maintain image quality in a higher-resolution image, the number of counts collected in each voxel must be maintained. With the number of resolution pixels increased by two times in all three dimensions or by an eight-time increment in the number of voxels, the counts recorded by the detector system should be increasing by eight times. This can be accomplished by increasing the axial field of view (AFOV) by about $8^{1/2}$ times or more, assuming the accidental and scatter fractions are constant. Hence, to effectively achieve a two times improvement in PET resolution to approach the fundamental limit of PET imaging without increasing image noise, it is necessary to have higher-resolution detector designs, with half the detector crystal size and a 2.8 times increase in AFOV, from the current 20 to 56 cm.

5.5 Higher Spatial Resolution Detector Designs

(a) PMT-based PET detector design. For high-resolution PET/CT, PMT is a cost-effective photodetector to assess the light from the scintillation crystals because of its large surface area in comparison to the SiPM. PMT is still being utilized in the current clinical whole-body PET/CT systems. As shown in Fig. 5.1, the common detector design for clinical PET systems is the block detector design, which consists of an array or a block of small scintillation crystal elements coupling to four PMT units. When a detector block senses a gamma ray, the location of the scintillating crystal element where the interaction occurs is determined, by the Anger analog-decoding scheme [14]. This block detector design can decode detector crystal size of 6×6 mm^2 with the low light output

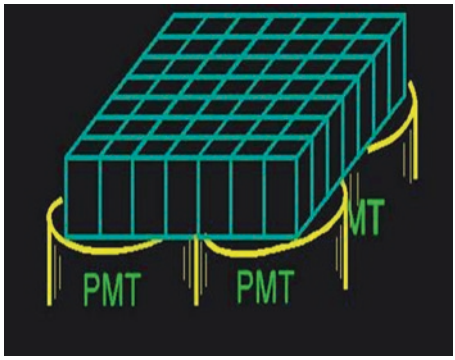

Fig. 5.1 Traditional block detector design in clinical PET/CT systems

BGO crystals and 4 × 4 mm^2 with L(Y)SO crystals which has four times more scintillation light output than BGO. These crystal sizes give rise to the 4–6 mm image resolution in current clinical PET and PET/CT systems. As discussed in the last section, the fundamental PET resolution limit for soft tissue is 2–3 mm for the large whole-body PET and 1–2 mm for a small brain PET system. However, it is possible to further improve the clinical PET imaging resolution from the current 4 to 6 mm.

Figure 5.2 shows that a new ultrahigh-resolution whole-body PET/CT has been developed, using the photomultiplier-quadrant-sharing (PQS) detector design [15–17]. This PQS detector design successfully decoded detector crystal blocks with 16 × 16 L(Y)SO crystals of 2.35 × 2.35 mm^2 (15.2 mm deep), using a very large PMT with 39 mm diameter [7]. This PQS detector-based whole-body PET/CT has achieved an image resolution of 2.8 mm, using the 3D filtered back-projection reconstruction and 1.4 mm resolution with the OSEM-PSF reconstruction [7]. The time-of-flight (TOF) resolution was 473 ps [18]. With a small detector diameter ring to reduce the non-colinearity effect, image resolution of 1 mm has also been achieved with the PQS detector design [17, 19], which would be useful for building dedicated brain PET systems. Hence, the PQS detector-based PET/CT systems can provide PET image resolution approaching the fundamental limit of PET imaging. The clinical images of the ultrahigh-resolution PET/CT system will be presented later in this chapter.

(b) *Silicon photomultiplier (SiPM)-based PET detector designs*. Unlike the 20–40 mm diameter PMT, the small SiPM photosensors allow each scintillation crystal element as small as 1 mm to be coupled to an individual SiPM, without using analog-position decoding as in the PMT-based PET detector designs. As a result, ultrahigh-resolution PET detectors approaching the fundamental PET resolution can be conceptually achieved with SiPM as photosensors. As discussed earlier, one of the disadvantages of SiPM is the higher cost of the numerous SiPMs and their individual processing electronics to cover the same

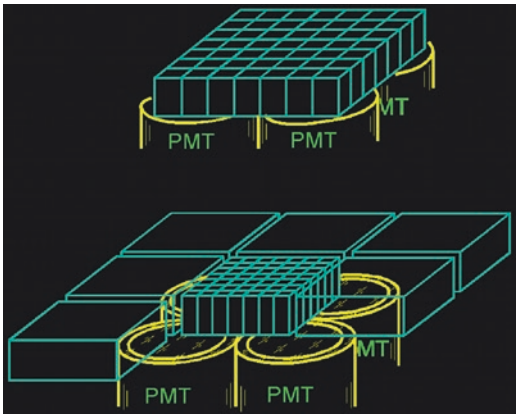

Fig. 5.2 *Upper*: traditional PET block detector design using four PMT to decode the crystal location. *Lower*: the PMT-quadrant-sharing detector design using four one-quadrant of four PMT to decode the crystal location while reducing the crystal and block size by half to improve imaging spatial resolution by two times in each dimension of the imaging space

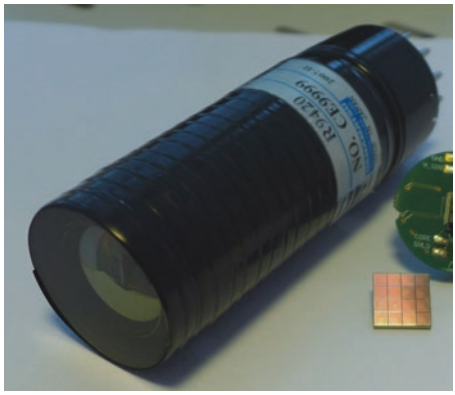

Fig. 5.3 One PMT and 16 SiPM units in a 4 × 4 array

crystal footprint of one PMT (Fig. 5.3). Namely, 81–144 SiPM (3–4 mm in size) are needed to replace a single 38-mm PMT used in clinical PET systems. Due to lower gain and higher noise, each SiPM channel requires its own amplifier and supporting electronics. Replacing a PMT with a 100 SiPM increases the processing electronics by a 100-fold, which further increases the production cost and substantially enhances the heat generation, thus requiring much better cooling. For building affordable and practical whole-body PET systems, the number of SiPM used needs to be reduced, which leads to the need of some form of analog decoding. Currently, SiPM-based PET/CT technology is still evolving to make it more affordable and practical, cost competitive, and performance competitive with PMT-based PET/CT systems. For PET/MR systems, SiPM with its magnetic field immunity is the only option, which ultimately contributes to the high cost of PET/MR systems.

In comparison to the PMT-based clinical PET/CT systems, with an image resolution of 2.8–6 mm [7, 20–22], commercial clinical PET/MR systems have PET resolution in the range of 3–4 mm [8–10]. The resolution of the PET in PET/MR systems using small SiPM is still short of the fundamental PET resolution limit of (1–2 mm). With future development of more cost-effective SiPM-based PET detector designs, ultrahigh-resolution PET/MR, and PET/CT approaching the fundamental limit can be achieved.

5.6 Improving PET Resolution with Depth-of-Interaction Positioning

Even with the high stopping power, scintillation crystals such as BGO and L(Y)SO, PET detectors need to be deep or thick (15–30 mm) to efficiently detect the energetic 511 KeV gamma rays. The deep detectors coupled with the coincidence detection of PET and the PET's detector ring geometry radially broaden the point spread function (resolution) (Fig. 5.4). The radial resolution worsens with deeper detectors

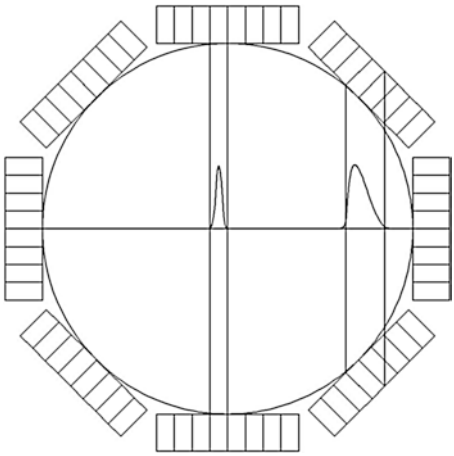

Fig. 5.4 The coincidence line-of-response point spread function widens with deep detectors in a ring geometry

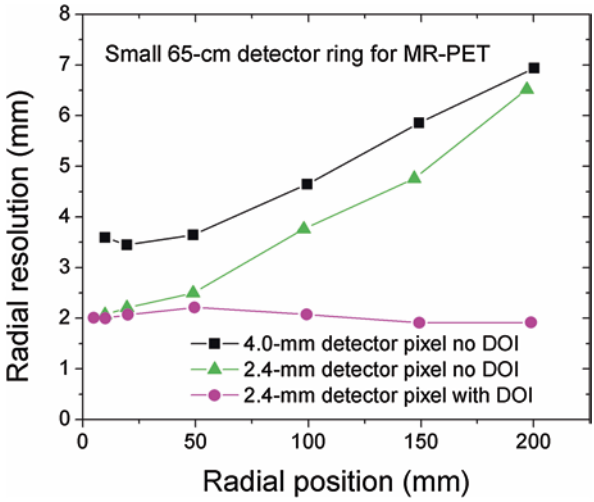

Fig. 5.5 Monte Carlo simulation of a small 65-cm PET detector ring. The 4-mm detector (20 mm deep) has resolution that degrades from 3.5 mm at center to 7 mm at position of 200 mm. The 2.4-mm detector (20 mm deep) has its resolution that degrades from 2 to 6.5 mm

and a smaller detection ring, despite the fact that PET detection sensitivity can be improved with deeper detectors and smaller detection rings (Fig. 5.5). As depicted in Fig. 5.6, such depth-of-interaction (DOI) resolution degradation also affects the axial resolution with a large axial field of view (AFOV), despite the fact that a large AFOV significantly increases PET's true count sensitivity to $(AFOV)^2$. If the DOI of a detected gamma ray can be measured, both the transaxial and the axial resolution of PET can be improved. Furthermore, in ultrahigh-resolution PET systems that have very narrow detectors of 1–2 mm^2, the DOI resolution degradation effect of deep crystals of 15–30 mm becomes more significant. Hence, it is essential to measure the DOI in ultrahigh-resolution and high sensitivity PET systems.

The classic DOI PET detector design is the dual-end DOI that has one solid-state photosensor such as SiPM, coupled to each end of the deep scintillation detector

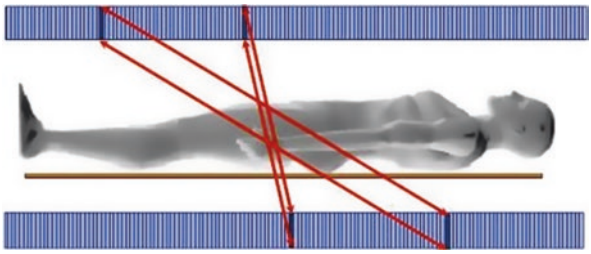

Fig. 5.6 The coincidence PSF worsens with large AFOV that can increase sensitivity significantly

pixel [23, 24], and the depth of interaction is derived from the difference in scintillation signals received by the two photosensors. This design can achieve DOI resolution of 2 mm, but it is costly to be implemented into a large clinical PET system, as it doubles the already large number of photosensors and supporting electronics.

Notably, there is no clinical whole-body PET system with DOI sensing at the present time. However, DOI sensing is important for providing the highest possible resolution in PET imaging. There are ongoing developments to engineer more practical DOI PET detectors, using fewer SiPMs by means of decoding schemes [25, 26] and a monolithic crystal block design [27]. Another direction of resolving the DOI degradation is using iterative image reconstruction that incorporates the system DOI degradation model and the detection point spread function to deconvolute the DOI effect in the estimated image [28, 29], which is also known as the high-definition (HD) image reconstruction. However, the HD iterative reconstructions may produce image edge artifacts [30].

Because of the importance of DOI sensing to improve PET resolution and facilitate large axial FOV PET that significantly improve PET sensitivity, DOI sensing PET will be a reality in the future.

5.7 Time-of-Flight Data Acquisition

By measuring the difference in the time of arrival of the two coincidence gamma rays, the location of the positron annihilation site can be estimated, which would improve the image quality (noise), which is equivalent to an increase in the effective detection sensitivity of PET. The timing uncertainty of this measurement is called the time-of-flight (TOF) resolution. In current clinical PET/CT that uses L(Y)SO crystals, the TOF resolution is about 390–525 ps in clinical PET/CT and PET/MR systems [8–10], depending on the speed of the photosensors, the efficiency of capturing scintillation light in the detector, and the accuracy of the electronic time-digital converter. The TOF positron localization uncertainty is 7.5 cm with a TOF resolution of 500 ps, which has been estimated to improve the effective PET detection sensitivity by 1.5–3 times [7, 21, 22]. Such sensitivity improvement depends on the patient size, the body cross section, and the metric of measuring this

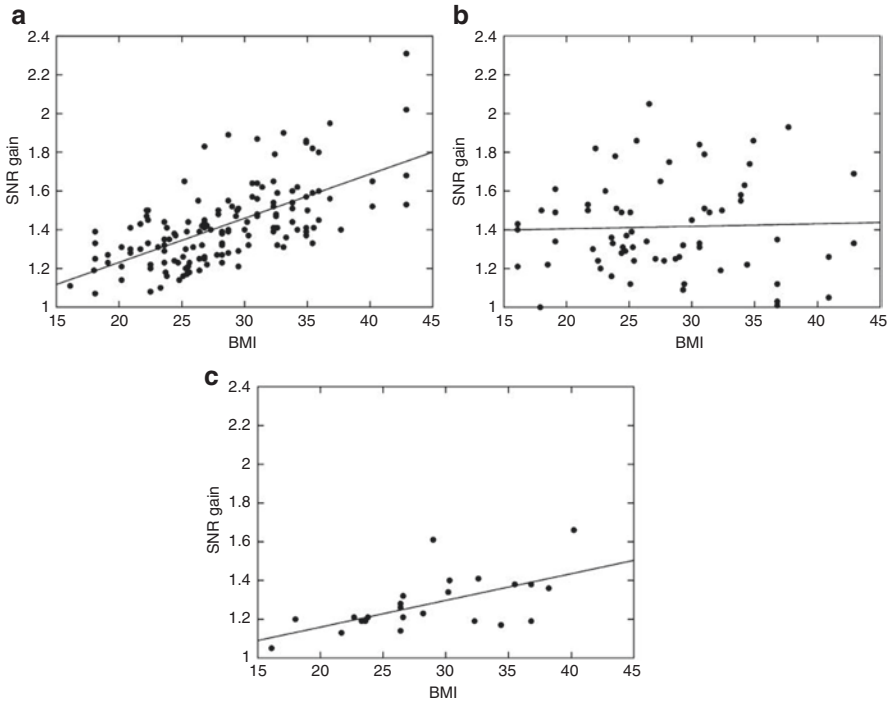

Fig. 5.7 Measured SNR gain factor vs. BMI, for small lesions (<2 cm) in different parts of the body for a group of 100 patients: (**a**) 144 lesions located in the abdomen, (**b**) 67 lesions located in the lung, and (**c**) 30 lesions located in the head and neck (This research was originally published in JNM by C. Lois et al. [34])

effective gain. Using LaBr scintillation crystals, the TOF resolution can be improved to below 400 ns translating to a positron localization uncertainty < 6 cm [31]. However due to the low photofraction of LaBr, the three times reduction in coincidence-detection sensitivity relative to L(Y)SO crystals (see Sect. 5.2), the loss in detection sensitivity of LaBr may exceed the higher TOF resolution gain relative to L(Y)SO, as a result of the low atomic number (Z). Relative to the low-cost BGO, LaBr suffers a 5.7 times reduction in first interaction photoelectric coincidence-detection sensitivity.

The advantage of TOF PET systems has been well demonstrated and quantified in phantom studies [32, 33]. For general clinical use, the TOF advantage is real but has more variability [34]; Fig. 5.7 shows that the average TOF gain in signal-to-noise ratio (SNR) was 1.1–1.3 times for the head, which corresponds to 1.2–1.7 times in sensitivity (Fig. 5.7). For the lung, the average SNR gain was 1.4 times, corresponding to a sensitivity gain of two times. The largest TOF gain was found in the abdomen, with SNR gain of 1.2–1.6 times depending on the body mass index (BMI), which is equivalent to 1.4–2.6 times increase in detection sensitivity. For the

predominant clinical PET of whole-body cancer staging application, the overall average effective TOF sensitivity gain that equals (SNR gain)^2 is approximately two times, which corresponds to a reduction in scan time by 50%.

5.8 Large Axial Field-of-View PET Camera

Increasing the AFOV is an effective means to significantly improve the count starvation characteristics of PET imaging because PET detection sensitivity is proportional to (AFOV)^2. The same effective sensitivity gain of two times from the current TOF PET/CT may be accomplished by increasing the axial field of view (AFOV) by 1.4 times. The current mainstream clinical PET/CT systems have AFOV of 20 cm. If this AFOV is increased from the current 20–25 cm to 1–1.2 m, it would cover the head and torso of more than 95% of the US male population [35], and detection sensitivity would be increased by 25 times from current commercial clinical PET/CT systems [36, 37]. The order of magnitude increase in sensitivity can be deployed in the following ways: (a) it can reduce the whole-body imaging time to 1–2 minutes with the current whole-body cancer staging clinical protocol of imaging one time at 30–45 min postinjection of FDG. This would significantly increase the clinical patient throughput to lower PET/CT imaging cost. Furthermore, a short one-minute imaging would significantly reduce patient movement comparing to a 30 min scan time, thereby substantially reducing artifacts from patient movements. (b) It would significantly reduce the image noise to provide much more accurate quantitation of molecular activities and significantly lower the molecular concentration levels that can be detected, which is important for imaging receptors and small lesions; and (c) current 20-cm AFOV PET/CT systems prevent dynamic imaging of the whole body, as the system has to step through 5–7 body sections at different times to image the whole body. The long AFOV PET/CT will enable whole-body dynamic tracer uptake imaging, assessing the entire body at exactly the same time. Studies have shown that a long AFOV PET will increase the effective detection sensitivity (EDS)* by 20–40 times [36, 37] depending on the AFOV size and crystal type, thus enabling the capture of changing time activity of tracers for the entire body.

Dynamic imaging is the only way to obtain quantitative physiology parametric (QPP) images for the entire body [38–44]. QPP images are more consistent among different clinical sites, which may reduce the barriers of multicenter studies and cross-center references. Hence, an affordable long AFOV PET may unleash the full potential of PET to study human physiology and quantitative molecular functions. It is particularly useful for studying the systemic whole-body therapy effects of drugs and their whole-body toxicity for normal tissues. Other advantages of a long AFOV PET that cover the whole torso and head are:

(1) The whole-body PET cancer staging imaging takes 20 min (3 min for 6–7 bed positions) with a 10 mCi of FDG injection, in which time and dosage can be respectively reduced to 1–2 min and 5 mCi. Since accidental coincidence noise

is proportional to (radioactivity)^2, reducing dose by 1/2 would reduce accidental noise by four times [45]. Hence, the system would improve image quality, lower the patient exposure to radiation by half, and shorten imaging time by ten times.

(2) High patient throughput: Assuming that the 1-m PET takes 2-min imaging plus 8 min for patient preparation (10 min total), compared to the current protocol of 20 min + 8 min + bed movement time for seven positions (30 min), patient throughput can be increased by more than three times.

(3) With 10 min/patient throughput and a 5 mCi dose per patient, the current "unit dose" of 10 mCi used for one patient can be used for two patients, since there is little radio decay for FDG after 10 min. Coupling this two times reduction in FDG cost to the two times higher patient throughput, the cost of cancer staging by PET would be substantially reduced.

(4) A 20 times increase in detection sensitivity will proportionally increase the counts per image pixel and facilitate the imaging of low-level receptor studies and other reaction studies, which are not currently achievable. For FDG dynamic studies, a 20 times increase in counts/pixel would produce whole-body metabolic rate images. Such images will have much higher accuracy when the counts in each pixel can be processed by the Patlak method or the 3-compartment model curve fitting process to yield whole-body images of the metabolism rate constants [41, 43, 44], without relying on the tedious and less revealing ROI drawings in each region to get enough count statistics.

5.9 Current State-Of-The-Art High-Resolution Clinical PET/CT Imaging

The recently developed high-resolution clinical PET/CT can provide image resolution of 2.9 mm with 3D filtered back-projection reconstruction (NEMA standard) and 1.4 mm when PSF iterative reconstruction is used [7]. The high-resolution brain images from 8-min to 20-min patient studies are shown in Figs. 5.8 and 5.9, respectively. Figure 5.8 shows brain images in transaxial, coronal, and sagittal directions, whereas Fig. 5.9 depicts nine contiguous slices of the transaxial image set with a fine axial sampling of 1.2 mm and 2.4 mm slice thickness from the high-resolution PQS PET detector system, which reveals small structural changes from slice to slice. Figure 5.10 compares the high-resolution PET image with the MR T1-weighted brain images of the same patient. The high-resolution PET images from this clinical PET/CT closely resemble that of the T1-weighted MR images from a 1.5 T MRI system, demonstrating that the recently developed high-resolution clinical PET system is capable of imaging the molecular features of small anatomic structures in the body.

In conclusion, while clinical PET technology has advanced a long way in the last 30 years, the full potential of PET imaging remains to be completely grasped**.** Current PET detector technology can achieve PET resolution approaching 1 mm or

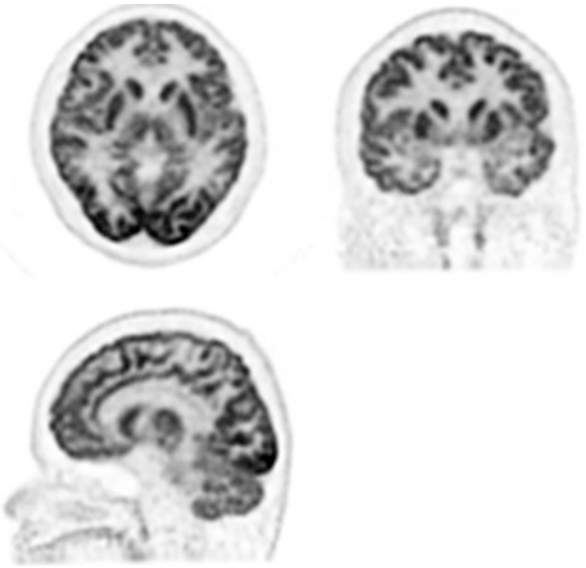

Fig. 5.8 Transverse, coronal, and sagittal views of a human brain imaged for 8 minutes with an ultrahigh-resolution PET/CT system with 2.8 mm resolution

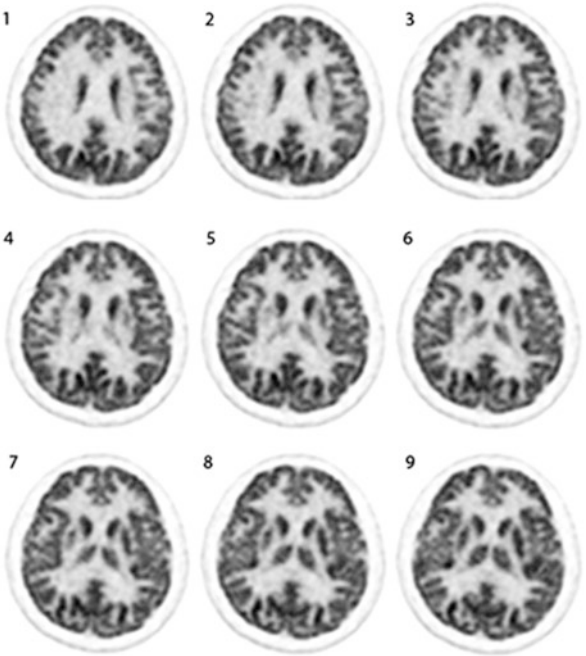

Fig. 5.9 Nine contiguous transverse images of a human brain with 20-min imaging. The slice-sampling spacing was 1.2 mm. Subtle changes in the brain structures between slices can be observed with the high-resolution axial sampling

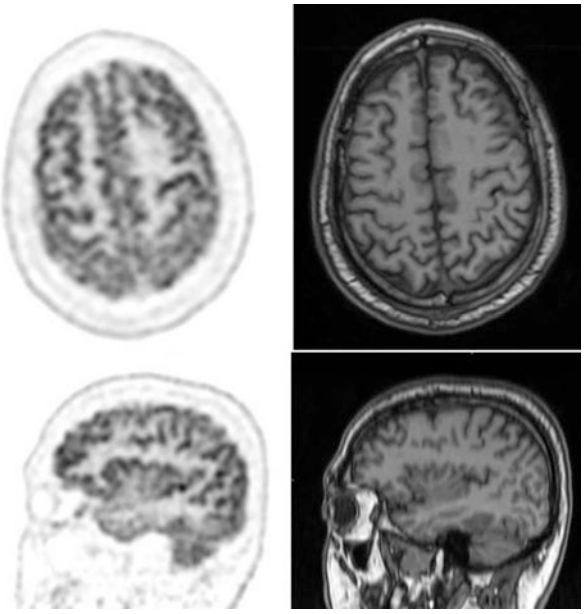

Fig. 5.10 The brain PET image from an 8-min PET acquisition (*left*) comparing with the T1-weighted MRI image from a 1.5 T MRI system (*right*) on the same human subject and the same brain slice

even smaller, using either the traditional PMT or the new SiPM photosensors. The bottleneck hindering the realization of the full potential of high-resolution PET imaging is the deficiency in detection sensitivities that the current time-of-flight technology alone cannot adequately overcome. This would require the axial field of view of PET to be economically extended multiple times to cover the preferable whole torso or more.

References

1. Melcher CL. Scintillation crystals for PET. J Nucl Med. 2000;41:1051–5.
2. Lewellen TK. Recent developments in PET detector technology. Phys Med Biol. 2008;53(17):R287–317.
3. Chinn G, Levin C. A maximum NEC criterion for Compton collimation to accurately identifying true coincidences in PET. IEEE Trans Med Imaging. 2011;30(7):1341–52.
4. van Loef EVD, Dorenbos P, van Eijk CDE, Kraemer KW, Guedel HU Appl Phys Lett. 2001;79:1573.
5. Daube-Witherspoon ME, Surti S, Perkins A, Kyba CCM, Wiener R, Werner ME, Kulp R, Karp JS. Imaging performance of a $LaBr_3$ based PET scanner. Phys Med Biol. 2010;55(1):45–64.
6. Wong W-H, Li H, Baghaei H, Zhang Y, Ramirez RA, Liu S, Wang C, An S. Engineering and performance (NEMA and Animal) of a lower-cost higher-resolution animal PET/CT scanner using photomultiplier(PMT)-quadrant-sharing detectors. J Nucl Med. 2012;53(11):1786–93.
7. Wong W-H, Li H, Zhang Y, Ramirez R, An S, Wang C, Liu S, Dong Y, Baghaei H. A high-resolution time-of-flight clinical PET detection system using gapless PMT-quadrant-sharing method. IEEE Trans Nucl Sci. 2015;62(5):2067–74.

8. Delso G, Fürst S, Jakoby B, Ladebeck R, Ganter C, Nekolla SG, Schwaiger M, Ziegler S. Performance measurements of the Siemens mMR integrated whole-body PET/MR scanner. J Nucl Med. 2011;52(12):1914–22.
9. Grant AM, Deller TW, Khalighi MM, Maramraju SH, Delso G, Levin CS. NEMA NU 2-2012 performance studies for the SiPM-based TOF-PET component of the GE SIGNA PET/MR system. Med Phys. 2016;43(5):2334–43.
10. Schug D, Wehner J, Dueppenbecker PM, Weissler B, Gebhardt P, Goldschmidt B, Salomon A, Kiessling F, Schulz V. PET performance and MRI compatibility evaluation of a digital, ToF-capable PET/MRI insert equipped with clinical scintillators. Phys Med Biol. 2015;60(5):7045–67.
11. Partridge M, Spinelli A, Ryder W, Hindorf C. The effect of β+ energy on performance of a small animal PET camera. Nucl Instrum Methods Phys Res A. 2006;568:933–6.
12. Jødall L, Loirec C, Champion. Positron range in PET imaging: an alternative approach for assessing and correcting the blurring. Phys Med Biol. 2012;57(5):3931–43.
13. Kengo Shibuya, Member, IEEE, Eiji Yoshida, Fumihiko Nishikido, Toshikazu Suzuki, Naoko Inadama, Taiga Yamaya, Hideo Murayama. A healthy volunteer FDG-PET study on annihilation radiation non-collinearity. In: IEEE Nuclear Science Symposium 2006 conference record. 1986. p. M06–7.
14. Casey ME, Nutt R. A multicrystal two dimensional BGO detector system for positron emission tomography. IEEE Trans Nucl Sci. 1986;33(1):460–3.
15. Wong W-H. A positron camera detector design with cross-coupled scintillators and quadrant sharing photomultipliers. IEEE Trans Nucl Sci. 1993;40(4):962.
16. Wong W-H, Uribe J, Hicks K, Zambelli M, Hu G. A 2-dimensional detector decoding study on BGO array with quadrant sharing photomultipliers. IEEE Trans Nucl Sci. 1994;41(4):1453–7.
17. Ramirez R, An S, Liu S, Zhang Y, Li H, Baghaei H, Wang C, Wong W-H. Ultra-high resolution LYSO PQS-SSS heptahedron blocks for low-cost MuPET. IEEE Trans Nucl Sci. 2011;58(3):626–33.
18. Li H, Wang C, An S, Lu X, Dong Y, Liu S, Baghaei H, Zhang Y, Ramirez R, Wong W-H. A fast and accurate timing alignment method with TDC linearity calibration for a high-resolution TOF-PET. IEEE Trans Nucl Sci. 2015;62(3):799–804.
19. Wong W-H, Li H, Baghaei H, Zhang Y, Ramirez RA, Liu S, Wang C, An S. Engineering and performance (NEMA and animal) of a lower-cost higher-resolution animal PET/CT scanner using photomultiplier(PMT)-quadrant-sharing detectors. J Nucl Med. 2012;53(11):1786–93.
20. Bettinardi V, Presotto L, Rapisarda E, Picchio M, Gianolli L, Gilardi MC. Physical performance of the new hybrid PET/CT discovery-690. Med Phys. 2011;38(10):5394–411.
21. Jakoby BW, Bercier Y, Conti M, Casey ME, Bendriem B, Townsend DW. Physical and clinical performance of the mCT time-of-flight PET/CT scanner. Phys Med Biol. 2011;56(10):2375–89.
22. Surti S, Kuhn A, Werner ME, Perkins AE, Kolthammer J, Karp JS. Performance of Philips Gemini TF PET/CT scanner with special consideration for its time-of-flight imaging capabilities. J Nucl Med. 2007;48(3):471–80.
23. Moses WW, Derenzo SE. Design studies for a PET detector module using a pin photodiode to measure depth of interaction. IEEE Trans Nucl Sci. 1994;41(4):1441–5.
24. Bircher C, Shao Y. Investigation of crystal surface finish and geometry on single LYSO scintillator detector performance for depth-of-interaction. Nucl Instrum Methods Phys Res A. 2012;693:236–43.
25. Zhang Y, Yan H, Baghaei H, Wong W-H. A novel depth-of-interaction block detector for positron emission tomography using a dichotomous orthogonal symmetry decoding concept. Phys Med Biol. 2016;61:1608–33.
26. Yuxuan Zhang, Han Yan, Hossain Baghaei, Wai-Hoi Wong. Lower-cost depth-of-interaction PET detector designs using dichotomous-3D decoding. In: 2015 IEEE Nuclear Science Symposium and Medical Imaging conference in San Diego, conference record. 2015.

27. Van Dam HT, Seifert S, Vinke R, Dendooven P, Lohner H, Beekman FJ, Schaart DR. A practical method for depth of interaction determination in monolithic scintillator PET detectors. Phys Med Biol. 2011;56:4135–45.
28. Panin VY, Kehren F, Michel C, Casey ME. Fully 3-D PET reconstruction with system matrix derived from point source measurements. IEEE Trans Med Imag. 2006;25:907–21.
29. Comtat C, Bataille CF, Michel C, et al. OSEM-3D reconstruction strategies for the ECAT HRRT. In: IEEE Medical Imaging conference record. Rome, Italy; 2004. P. 3492–96.
30. Reimold M, Pfannenberg C, Kupferschläger J, Bares R. High resolution image reconstruction (point spread function based) in FDG brain PET. J Nucl Med. 2012;53 (Supplement 1):2341. 15. 6.
31. Karp JS, Kuhn A, Perkins AE, et al. Characterization of a time-of-flight PET scanner based on lanthanum bromide. In: IEEE nuclear science symposium conference record. 2005.
32. Karp JS, Surti S, Daube-Witherspoon ME, Muehllehner G. Benefit of time-of- flight in PET: experimental and clinical results. J Nucl Med. 2008;49:462–70.
33. Surti S, Kuhn A, Werner ME, et al. Performance of Philips Gemini TF PET/CT scanner with special consideration for its time-of-flight imaging capabilities. J Nucl Med. 2007;48:471–80.
34. Lois C, Jakoby BW, Long MJ, Hubner KF, Barker DW, Casey ME, Conti M, Panin VY, Kadrmas DJ, Townsend DW. An assessment of the impact of incorporating time-of-flight information into PET/CT imaging. J Nucl Med. 2010;51(2):237–45.
35. NASA Anthropometry and biomechanics, vol. 1, section3, Men-Systems Integration Standard. http://msis.jsc.nasa.gov/sections/section03.htm
36. Wong WH, Zhang Y, Liu S, Li H, Baghaei H, Ramirez R, An S, Wang C. Feasibility studies of an affordable high-resolution 1-meter long PET. J Nucl Med. 2008;49(Supplement 1):411.
37. Poon JK, Dahlbom ML, Moses WW, Balakrishnan K, Wang WL, Cherry SR, Badawi RD. Optimal whole-body PET scanner configurations for different volumes of LSO scintillator: a simulation study. Phys Med Biol. 2012;57(13):4077–94. 9.
38. Carson RE. Parameter estimation in positron emission tomography, positron emission tomography and autoradiograpy. In: Phelps ME, Mazziotta JC, Shelbert HR, editors. Raven Press; 1986. p. 347–90.
39. Huang SC, Phelps ME. Principle of tracer modeling in positron emission tomography and autoradiograpy, positron emission tomography and autoradiograpy. In: Phelps ME, Mazziotta JC, Shelbert HR, editors. Raven Press; 1986. p. 287–346.
40. Sokoloff L, Reivich M, Kennedy C, et al. The (14C)-deoxyglucose method for the measurement of local cerebral glucose utilization: theory, procedure and normal values in the conscious and anesthetized albino rat. J Neurochem. 1977;28:897–916.
41. Patlak CS, Blasberg RG, Fenstermacher JD. Graphical evaluation of blood to brain transfer constants from multiple time uptake data. J Cereb Blood Flow Metab. 1983;3:1–7.
42. Gjedde A. Calculation of glucose phosphorylation from brain uptake of glucose analogs in vivo: a re-examination. Brain Res Rev. 1982;4:237–374.
43. Wong WH, Hicks K. A clinically practical method to acquire parametric images of unidirectional metabolic rates and blood space. J Nucl Med. 1994;35(7):1206–11.
44. Kimura Y, Senda M, Alpert NM. Fast formation of statistically reliable FDG parametric image based on clustering and principal components. Phys Med Biol. 2002;47:455–68.
45. Hoffman EJ, Phelps ME. Positron emission tomography principles and quantitation. In: Phelps M, Maaziotta JC, Schelbert HR, editors. Positron emission tomography and autoradiography: principles and applications for the brain and heart. New York: Raven; 1986. p. 237–86.